

Enhanced electrical conductivity of transparent electrode using metal microfiber networks for gridless thin-film solar cells

Dae-Hyung Cho^{a,b}, Hong Seok Jo^c, Woo-Jung Lee^a, Tae-Gun Kim^c, Byungha Shin^{b,***},
Sam S. Yoon^{c,**}, Yong-Duck Chung^{a,d,*}

^a ICT Materials & Components Research Laboratory, Electronics and Telecommunications Research Institute (ETRI), Daejeon 34129, South Korea

^b Department of Materials Science and Engineering, Korea Advanced Institute of Science and Technology (KAIST), Daejeon 34141, South Korea

^c School of Mechanical Engineering, Korea University, Seoul 02841, South Korea

^d Department of Advanced Device Technology, Korea University of Science and Technology (UST), Daejeon 34113, South Korea

ARTICLE INFO

Keywords:

Thin-film solar cells
Ni fibers
Transparent electrodes
Gridless

ABSTRACT

Improving the optical transmittance and electrical conductivity in transparent conductors (TC) has been a critical issue for decades due to their numerous applications. In this paper, we suggest an approach to produce extremely conductive TC material from electroplated Ni microfiber networks (NiMFs) in order to achieve highly efficient and aesthetically superior thin-film solar cells and modules. The high cross-sectional aspect ratio of NiMFs significantly enhanced their electrical conductivity and optical transmittance simultaneously. The TC structure employing NiMFs was a successful substitute for conventional patterned grids in Cu(In,Ga)Se₂ thin-film solar cells because it reduced the series resistance, which is especially advantageous for large-area cells. The NiMF-induced transmittance loss was compensated for by the formation of a light diffusion layer on the NiMF. We propose that the excellent performance of NiMF TC materials enables the elimination or significant reduction of the grids in thin-film solar cells and modules.

1. Introduction

Transparent conductors (TCs) have been widely used as electrodes in either light-absorbing or light-emitting devices such as thin-film solar cells, displays, sensors, and e-paper [1]. Various approaches are being used to simultaneously achieve a high optical transmittance and electrical conductivity using transparent conducting oxides (TCOs), ultra-thin metals, or nano-scale conducting materials such as silver nanowires (AgNWs), graphene, and carbon nanotubes [2–14]. Highly efficient Cu(In,Ga)Se₂ (CIGS) thin-film solar cells usually include TCO thin films, which typically include impurity doped-zinc oxide (ZnO) or indium tin oxide (ITO), as a TC electrode [15,16]. The TCO used in CIGS thin-film solar cells must have high transmittance and low resistance in order to improve light absorption and carrier transport efficiency, respectively. Because of their large sheet resistance (R_{sh} , tens of $\Omega\text{-sq}^{-1}$), it is difficult for generated electrons to travel long distances through only the TCO films; therefore, CIGS thin-film solar cell and module manufacturers usually employ a monolithic integration process to

reduce the travel length of electrons [17]. However, this process is challenging to apply to flexible substrates because the metallic foils require high-quality insulation layers and the structuring processes do not fit well with roll-to-roll processing [18,19]. Thus, front grids including busbar and finger patterns are generally used in commercial flexible CIGS photovoltaics [20–22]. A multi-busbar metal grid is also used in highly efficient crystalline silicon solar modules [23]. Millimeters-wide metal grids are typically used to achieve a high electrical conductance. These wide grid patterns inevitably block light and are obtrusive, making them unsuitable for applications involving building integrated photovoltaic and portable devices. Because the geometries of grid patterns (width, length, and gap) and cell dimensions are typically optimized considering the R_{sh} of the TC material in order to minimize the area of the fraction of the grid [24,25], the resistance of the TC should be significantly reduced to lessen (or remove) the area of the fraction of the grid. Metal fibers can be a viable alternative for achieving a very high cross-sectional aspect ratio compared to film-type metal grids, which enable a high aperture ratio and low resistance.

* Corresponding author. ICT Materials & Components Research Laboratory, Electronics and Telecommunications Research Institute (ETRI), Department of Advanced Device Technology, Korea University of Science and Technology (UST), Daejeon 34113, South Korea.

** Corresponding author.

*** Corresponding author.

E-mail addresses: byungha@kaist.ac.kr (B. Shin), skyoona@korea.ac.kr (S.S. Yoon), ydchung@etri.re.kr (Y.-D. Chung).

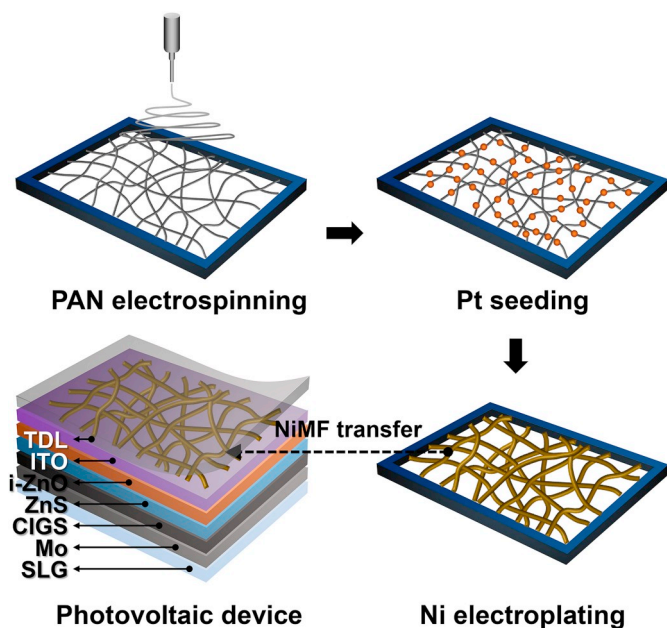


Fig. 1. Schematic of processes of NiMF fabrication and transfer onto CIGS thin-film photovoltaic device. The NiMF is prepared by sequential processes: PAN electrospinning, Pt seeding, and Ni electroplating, and then transferred onto photovoltaic devices of ITO/i-ZnO/ZnS/CIGS/Mo/SLG structure.

Although nano-scale metal fibers or wires have been extensively studied, their low cross-sectional area and large surface area limit the further improvement of their resistivity and chemical stability, respectively [26–29]. Therefore, micro-scale fibers made from corrosion-resistant material can provide a good alternative for conventional nanostructured networks. Although highly transparent and conductive metal fibers have been demonstrated in previous reports [30–32], there are few studies on their application of front contacts in thin-film solar cells. In this study, we fabricated extremely conductive Ni microfiber networks (NiMFs) and applied them to CIGS solar cells in order to improve their performance and eliminate patterned grids. The performance gains of bare NiMF and NiMF-employed CIGS photovoltaic devices are discussed. We found that NiMFs have great potential to replace conventional patterned metal grids.

2. Experimental procedures

The NiMFs were fabricated through the following steps, as shown in Fig. 1. First, an 8 wt% polyacrylonitrile (PAN, Mw = 150 kDa, Sigma-Aldrich, USA) solution with N,N-dimethylformamide (DMF, 99.8%, Sigma-Aldrich, USA) as the solvent was electrospun onto a flat collector for 2 s; the flow rate of the solution was maintained at $200 \mu\text{L h}^{-1}$ using a needle (25 gauge, EFD, USA) and syringe pump (Legato 100, KD Scientific, USA). The voltage for electrospinning was maintained at 5 kV using a DC high-voltage supply (EL20P2, Glassman High Voltage, USA). Subsequently, the electrospun PAN nanofibers (PAN NFs) with diameters of ~ 250 nm were transferred to a square copper frame with dimensions of $3 \text{ cm} \times 2 \text{ cm}$. Pt seeds were sputtered onto the PAN NFs for electroplating, then Ni was electroplated onto the seeded PAN NFs at a voltage of 6 V for different electroplating times ($t_{\text{EP}} = 20 \text{ s}$, 25 s , and 30 s). The electroplating time is related to the diameter of the NiMFs. The NiMFs were washed with distilled water and fully dried under N_2 for a few minutes. Finally, the fabricated NiMF networks were detached from the frame and transferred onto a solar cell structure of ITO/i-ZnO/ZnS/CIGS/Mo/soda-lime glass (SLG). The solar cell samples used in this work were prepared in the identical batch at each process step. In order to improve the contact between the NiMFs and the ITO surface, the NiMFs were covered with $56\text{-}\mu\text{m}$ -thick commercial

adhesive tape (Scotch[®] Magic[™] Tape, 3M, USA). Since the adhesive tape is highly transparent and hazy, it is referred to as a transparent diffusive layer (TDL). To fabricate the CIGS solar cells, the CIGS absorber film was co-evaporated using our baseline process on Mo-coated SLG substrates, as reported elsewhere [33–37]. The CIGS layers were coated with an environmentally friendly ZnS buffer layer using a chemical bath deposition method, avoiding CdS-containing materials, which include highly toxic Cd. Highly resistive i-ZnO and highly conductive ITO thin films were deposited via rf sputtering in the same chamber.

The morphology of the fabricated NiMFs was observed using scanning electron microscopy (SEM, SU8230, Hitachi, Japan). The total and diffusive transmittances were determined using a UV-VIS spectrophotometer with an integrating sphere (Lambda 1050, PerkinElmer, USA). The R_{sh} values were obtained using a four-point probe measuring system (CMT-SERIES, Chang Min Co., Ltd., Korea). The current density–voltage (J - V) characteristic of the CIGS solar cells was measured using an I - V source meter (Keithley 2400, Tektronix, USA) under an Air Mass 1.5 global (AM 1.5 g) spectrum of 1000 W m^{-2} irradiance at room temperature. Before the J - V measurement, the solar cell areas were defined by mechanical scribing with electrical isolation. The external quantum efficiency (EQE) was measured via a spectrally resolved monochromatic light with a 12-W halogen lamp (Newport, USA). The solar cells were light-soaked under white light for 1 h before the J - V and EQE measurements [38].

3. Results and discussion

The optical transmittance and R_{sh} of the NiMFs with electroplating times of $t_{\text{EP}} = 20 \text{ s}$, 25 s , and 30 s were measured. Fig. 2(a) indicates that the diameters d of the NiMFs with the increasing t_{EP} values were $3.68 \mu\text{m}$, $4.88 \mu\text{m}$, and $5.84 \mu\text{m}$, respectively, exhibiting linear dependency on t_{EP} with a growth rate of $0.19 \mu\text{m/s}$. The interconnections were well fused because the micro-scale-thick Ni grew from the surface of the thin 250-nm -diameter PAN NFs, which was believed to minimize the electrical conductivity loss. The NiMFs were randomly distributed on the ITO film surface, as shown in Fig. 2(a).

As shown in Fig. 2(b), all NiMFs exhibited transmittances over 93% in the wide wavelength range from 300 nm to 1100 nm. Inevitably, the thinner NiMFs (shorter t_{EP}) exhibited a higher transmittance. The transmittance at a 500-nm-wavelength (T_{550}) of the NiMFs with a t_{EP} of 20 s, 25 s, and 30 s was 97.5%, 94.8%, and 93.1%, respectively. The R_{sh} of the same NiMFs was $2.35 \Omega \text{ sq}^{-1}$, $1.61 \Omega \text{ sq}^{-1}$, and $0.91 \Omega \text{ sq}^{-1}$, respectively. These significantly low R_{sh} values are attributed to the large volume and high cross-sectional aspect ratio (height-to-width) of the NiMFs compared with those of TC materials of other dimensions such as thin films and nanostructures. The diameter-dependent R_{sh} was simulated to estimate the d value required to achieve the desired R_{sh} values, as shown in Fig. 2(c). For a simpler calculation than that in the percolation theory [39], the NiMFs were assumed to be a two-dimensional rectangular network, as illustrated in the inset of Fig. 2(c). The R_{sh} as a function of d , according to Kirchhoff's rules, with $N \times N$ fibers, is given by

$$R_{\text{sh}} = \frac{N}{N+1} R_{\text{fiber}} = \frac{N}{N+1} \frac{\rho L_{\text{eff}}}{\pi \left(\frac{d}{2}\right)^2} \approx \frac{4\rho L_{\text{eff}}}{\pi d^2} \quad [40], \quad (1)$$

where R_{fiber} is the resistance of the unit length of a fiber, ρ is the resistivity of Ni, and L_{eff} is the effective length of a unit fiber (network pitch) [40]. $N/(N+1)$ is close to unity for large N values in these NiMFs. R_{sh} significantly decreased with diameter inversely proportional to d^2 , while it had a linear dependency on L_{eff} . The L_{eff} values of the NiMFs were calculated to be $190 \mu\text{m}$ using the following equation,

$$1 - T_{550} = AF = \frac{2d}{L_{\text{eff}}}, \quad (2)$$

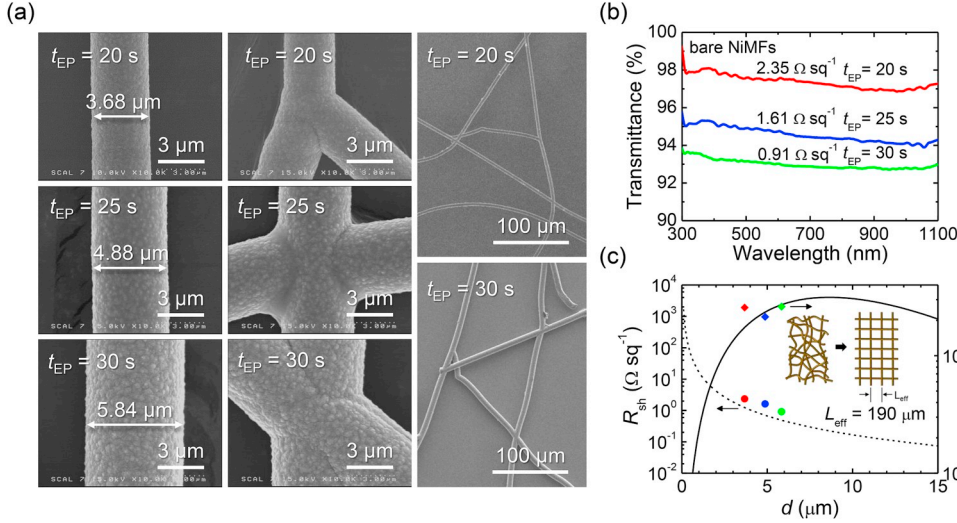


Fig. 2. (a) SEM images and (b) transmission spectra of NiMFs prepared with different electroplating times (t_{EP}). R_{sh} values are also shown. (c) Measured (solid circle) and simulated (dashed line, assuming $L_{eff} = 190 \mu\text{m}$) R_{sh} values as a function of the diameter d of the NiMFs. Measured (solid diamond) and calculated (solid line) Haacke's FOMs with $n = 20$ as a function of the diameter d of NiMFs are also plotted. The red, blue, and green symbols indicate the t_{EP} of 20, 25, and 30 s, respectively. The inset schematically indicates that the randomly distributed NiMFs were assumed to be a two-dimensional rectangular network. (For interpretation of the references to colour in this figure legend, the reader is referred to the Web version of this article.)

assuming the light was totally blocked by the NiMF, where AF is the area fraction of the NiMF over a unit area. The measured R_{sh} for each d value was higher than the calculated values because some of the NiMFs were cut or not totally connected to each other. Moreover, the deposited Ni was likely to be polycrystalline, which may induce electron reflection at the grain boundaries, resulting in an increased Ni resistivity [41,42]. Haacke's figure of merit (FOM) was also determined as a function of d using the equation T_{550}^{20}/R_{sh} , where $n = 20$, assuming the TC applications required a transmittance greater than 95% [43]. The highest FOM value was obtained at a d value of $8.6 \mu\text{m}$ which was comparable to the diameters of the fabricated NiMFs. The T_{550}^{20}/R_{sh} values, obtained using the measured T_{550} and R_{sh} , were in accordance with the calculated curve.

The NiMF samples were transferred onto an ITO/i-ZnO structure used as a window layer in CIGS solar cells. The optical and electrical properties of the different structures, TDL/NiMF-20s or NiMF-30s/ITO/i-ZnO/SLG and ITO/i-ZnO/SLG, were investigated and evaluated to determine their performances as TC materials using various FOMs. Although the addition of TDL/NiMF layers reduced the total transmittance of the whole wavelength range, the diffusive transmittance dramatically improved from 1% (without TDL/NiMF) to 50% (with TDL/NiMF), as shown in Fig. 3(a). The R_{sh} rapidly decreased with the application of NiMFs to ITO/i-ZnO. The NiMF-20s- and NiMF-30s-incorporated samples exhibited R_{sh} values of $1.34 \Omega \text{sq}^{-1}$ and $0.262 \Omega \text{sq}^{-1}$, respectively, as shown in Table 1. When fabricating the control solar cell sample using the ITO/i-ZnO structure, the patterned grid is formed on top of the solar cell.

In general, there is a trade-off between the transmittance and R_{sh} in TC materials, which is described by the following equation:

$$T = \left[1 + \frac{Z_0}{2R_{sh}} \left(\frac{\sigma_{DC}}{\sigma_{Opt}} \right)^{-1} \right]^{-2} = \left[1 + \frac{188.5}{R_{sh}} \left(\frac{\sigma_{DC}}{\sigma_{Opt}} \right)^{-1} \right]^{-2} \quad [44], \quad (3)$$

where σ_{DC} is the dc conductivity, σ_{Opt} is the optical conductivity, and Z_0 is the impedance of free space [44]. σ_{DC}/σ_{Opt} , known as the conductivity ratio, is often used as a FOM to evaluate TC material systems. The T_{550} as a function of R_{sh} for ITO/i-ZnO, NiMF, and TDL/NiMF/ITO/i-ZnO is plotted in Fig. 3(b). The dashed curves were obtained by considering various previously reported σ_{DC}/σ_{Opt} values. The σ_{DC}/σ_{Opt} of the NiMF-employed structures exceeded that of other TC materials, such as ITOs, AgNWs, patterned metals, and SWNTs [4,44–47]. The bare NiMFs exhibited an σ_{DC}/σ_{Opt} value of ~ 5000 . The TDL/NiMF/ITO/i-ZnO samples exhibited significantly higher σ_{DC}/σ_{Opt} values than ITO/i-ZnO, because of the significant improvement in R_{sh} . In the TDL/NiMF/ITO/i-ZnO structures, the NiMF-30s exhibited a much higher σ_{DC}/σ_{Opt} than the NiMF-20s because of the reduced R_{sh} with little loss in transmittance. However, the σ_{DC}/σ_{Opt} ratio only describes free carrier effects, making it unsuitable for use at wavelengths below the plasma wavelength [4].

To evaluate the potential applications for CIGS solar cells, other FOMs were calculated using the solar-weighted transmission (WT). Although T_{550} is widely used for estimating the degree of optical transmission in TC materials, the wavelength-dependent solar irradiance should be considered for evaluating solar cell performance. The WT was obtained using

$$WT(\lambda) = \frac{\int_{\lambda_1}^{\lambda_2} I_{AM1.5}(\lambda) T(\lambda) d\lambda}{\int_{\lambda_1}^{\lambda_2} I_{AM1.5}(\lambda) d\lambda}, \quad (4)$$

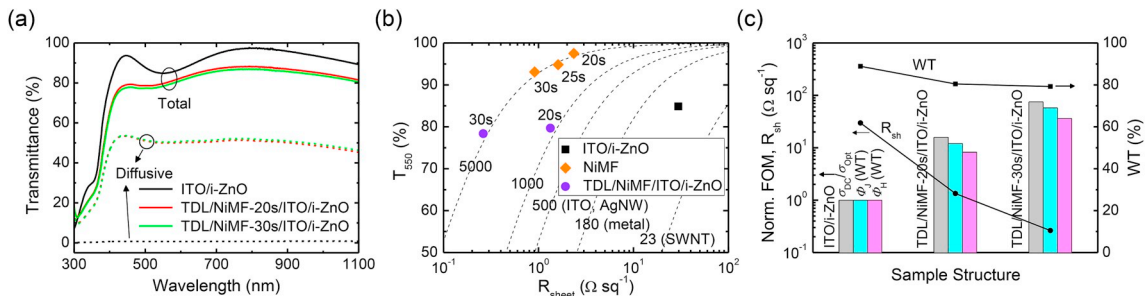


Fig. 3. Characteristics of three TC structures of ITO/i-ZnO, TDL/NiMF-20s/ITO/i-ZnO, and TDL/NiMF-30s/ITO/i-ZnO. (a) Total and diffusive transmittances as a function of wavelength. (b) T_{550} and R_{sh} values of various structures. Dashed lines indicate representative σ_{DC}/σ_{Opt} values from this work and other studies: ITO, AgNW, metal, and SWNT [4,44–47]. (c) Comparison of different FOMs of σ_{DC}/σ_{Opt} , Φ_J , and Φ_H , normalized by that of ITO/i-ZnO structure. The corresponding WT and R_{sh} are also shown.

Table 1

Measured sheet resistance (R_{sh}), solar-weighted transmission (WT), and transmittance at a 500-nm-wavelength (T_{550}) of ITO/i-ZnO, TDL/NiMF-20s/ITO/i-ZnO, and TDL/NiMF-30s/ITO/i-ZnO structures. The corresponding three FOMs: conductivity ratio (σ_{DC}/σ_{Opt}), Jain's (Φ_J), and Haacke's (Φ_H), and calculated J_{loss} induced by the TC materials are also listed.

Material	R_{sh} (Ω sq $^{-1}$)	WT	T_{550} (%)	σ_{DC}/σ_{Opt} (T_{550})	Φ_J (WT, Ω^{-1})	Φ_H (WT, $10^{-3}\Omega^{-1}$)	J_{loss} (mA cm $^{-2}$)
ITO/i-ZnO	29.7	88.86	84.87	74	0.285	10.33	4.49 (+ grid: 5.92)
TDL/NiMF-20s/ITO/i-ZnO	1.34	80.47	79.67	1169	3.43	84.96	8.19
TDL/NiMF-30s/ITO/i-ZnO	0.262	79.24	78.36	5548	16.4	372.5	8.75

where the $I_{AM1.5}(\lambda)$ is the wavelength-dependent AM 1.5G solar flux and $T(\lambda)$ is the wavelength-dependent transmittance of the TC material. The λ_1 and λ_2 values were set as 300 nm and 1200 nm, respectively, to cover the wavelength range of the spectral response of our CIGS solar cell [48]. The TDL/NiMF-20s and TDL/NiMF-30s materials resulted in transmittance reductions of about 8.4% and 9.6%, respectively, compared to the bare ITO/i-ZnO. The two different FOM definitions of the various TC structures, proposed by Haacke (Φ_H) [43] and Jain et al. (Φ_J) [49], were also calculated using the WT as follows:

$$\Phi_H = \frac{WT^{10}}{R_{sh}} \quad [43], \quad (5)$$

$$\Phi_J = \frac{\sigma}{\alpha} = - [R_{sh} \ln(WT + R)]^{-1} \quad [49], \quad (6)$$

where σ is the resistivity, α is the absorption coefficient, and R is the reflectance (neglected in this work) of the TC materials. Φ_H is the thickness-dependent that yields film property, whereas the Φ_J is the thickness-independent exhibiting the intrinsic material property. The three different FOMs calculated, σ_{DC}/σ_{Opt} , Φ_H , and Φ_J , are summarized in Table 1. The normalized FOMs of each of the TC structures (the FOM of the ITO/i-ZnO was 1) are plotted in Fig. 3(c). All the FOMs significantly increased after NiMFs were formed on the ITO/i-ZnO layers because of the significant reduction in the R_{sh} value. The FOMs were much higher than those of the high-quality ITO film and AgNWs [4]. The FOM of the NiMF-30s-employed sample was larger than that of the NiMF-20s-employed sample because of the improvement in the R_{sh} value with little loss in transmittance. For solar cell applications, the loss in the short circuit current (J_{loss}) was calculated as follows, in order to quantitatively estimate the effect of the transmittance loss, which was induced by the NiMFs, on the photovoltaic performances.

$$J_{loss} = \frac{q}{hc} \int_{\lambda_1}^{\lambda_2} I_{AM1.5}(\lambda)(1 - T(\lambda))d\lambda, \quad (7)$$

As a patterned metal grid was fabricated on the solar cells of the ITO/i-ZnO window layer, the shading factor of the grid (3.3%) is also considered. The additional J_{loss} induced by the TDL/NiMF-20s and TDL/NiMF-30s structures was about 2.3 mA cm $^{-2}$ and 2.8 mA cm $^{-2}$, respectively, compared with the grid/ITO/i-ZnO.

The different TC materials, patterned grid, TDL/NiMF-20s, and TDL/NiMF-30s, were prepared on the ITO/i-ZnO/ZnS/CIGS/Mo/SLG solar cell structures with dimensions of 25 mm \times 25 mm, as shown in Fig. 4(a). Every single solar cell was defined by mechanical scribing to obtain a designated 0.5 cm 2 illumination area [50]. The patterned grid includes 100- μ m-wide busbars and 25- μ m-wide fingers that are visible to the naked eye, although the NiMFs were non-obtrusive. The J - V characteristics are displayed in Fig. 4(b). By applying TDL/NiMF-20s instead of the patterned grid, the J_{SC} was improved by \sim 1.76 mA cm $^{-2}$, which is contrary to the calculated J_{loss} value in Table 1. The quantum efficiency was also improved for almost the entire wavelength region, as shown in Fig. 4(c). The enhanced J_{SC} was believed to be due to the significantly improved diffusive transmission because of the TDL, which

likely prolonged the optical path length in the CIGS absorber [51,52]. The TDL/NiMF-30s sample exhibited an improvement in the fill factor (FF) because of the low R_{sh} compared to that of the TDL/NiMF-20s sample, while the J_{SC} of the TDL/NiMF-30s sample decreased because of the lower transmittance. The J_{SC} values calculated from the EQE of the patterned grid, TDL/NiMF-20s, and TDL/NiMF-30s were 29.55 mA cm $^{-2}$, 30.45 mA cm $^{-2}$, and 28.48 mA cm $^{-2}$, respectively, which agreed well with the measured J_{SC} values. The differentiated EQE, $dEQE/d\lambda$, exhibited two peaks around wavelengths of 380 nm and 1030 nm (sharp edges in EQE), which indicate the energy band gaps corresponding to the ITO/i-ZnO/ZnS and CIGS layer, respectively. This means that the band gap property remained the same for the samples. The band gap of the CIGS absorber was estimated to be 1.20 eV.

We investigated the area-dependent solar cell efficiency with NiMFs with two different fiber thicknesses in order to examine the potential of applying the NiMFs to larger-area solar cells. Cell areas of approximately 2.25 cm 2 , 1.5 cm 2 , 1.0 cm 2 , and 0.5 cm 2 (shown in the inset of Fig. 5) were sequentially obtained via mechanical scribing. Because the cell areas were defined by manual mechanical scribing, the measured cell areas slightly differed from the desired areas. There was a negligible decrease in the solar cell efficiency (\sim 14.2%) of the NiMF-30s sample with increasing cell area, whereas that of the NiMF-20s sample decreased from 14.9% to 13.3%. The efficiency was largely affected by the decline in the FF in the area, which was due to the increase in R_{series} . The R_{series} of both NiMF-20s and NiMF-30s samples was \sim 0.9 Ω cm 2 over an area of 0.5-cm 2 , while it was 2.95 Ω cm 2 and 1.55 Ω cm 2 , respectively, over an area of 2.25 cm 2 . The R_{series} values were calculated by fitting the J - V curves using a two-diode model [53]. The J_{SC} hardly changed with the area, showing an average difference of 1.5 mA cm $^{-2}$ between the NiMF-20s and NiMF-30s samples, because of the difference in the transmittance of the fibers. The J_{SC} values for the 0.5 cm 2 area were slightly lower than those for the larger areas because the area fraction of the indium top contact increased for the smaller areas. Not surprisingly, the P_{max} value of the NiMF-20s became less than that of the NiMF-30s. Among the causes that determine the P_{loss} , the degree of the contribution of the TC materials and grids is expressed as

$$P_{loss} = \int I^2 dR = \int_0^{S/2} \frac{J^2 b^2 y^2 R_{sh} dy}{b} = R_{sh} \left[\frac{J^2 b S^3}{24} \right] \quad [54], \quad (8)$$

where J is the current density, and S , b , and y are factors related to the grid dimensions [54]. This equation indicates that P_{loss} is directly proportional to R_{sh} when the grid dimensions are unchanged. Since the grid dimensions (one round indium paste contact) were the same for each area and NiMF thickness, the larger P_{loss} (smaller P_{max}) of the NiMF-20s samples can be explained by the larger R_{sh} .

4. Conclusions

NiMFs with a high cross-sectional aspect ratio were fabricated via a facile and easily-scalable electroplating method. The NiMF greatly enhanced the electrical conductivity resulting in higher FOM values than those of conventional TC materials. The randomly distributed

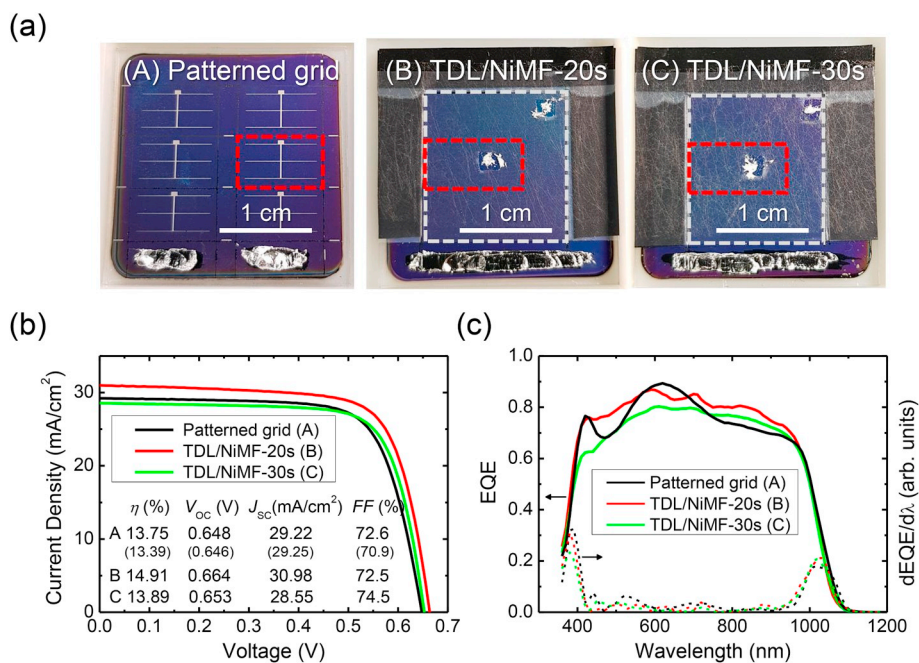


Fig. 4. (a) Pictures of fabricated solar cell devices terminated by the patterned grid (left, A), TDL/NiMF-20s (center, B), and TDL/NiMF-30s (right, C) onto ITO/i-ZnO/ZnS/CIGS/Mo/SLG structures. The red dashed lines indicate a cell area of $\sim 0.5 \text{ cm}^2$ for solar cell performance measurements. (b) Corresponding J - V curves of A, B, and C samples and their photovoltaic performances of efficiency (η), open circuit voltage (V_{oc}), short circuit current (J_{sc}), and fill factor (FF) (inset). The average parameter values of the six individual cells in the patterned grid sample (A) were indicated in brackets. (c) EQEs and differentiated spectra of samples A, B, and C. (For interpretation of the references to colour in this figure legend, the reader is referred to the Web version of this article.)

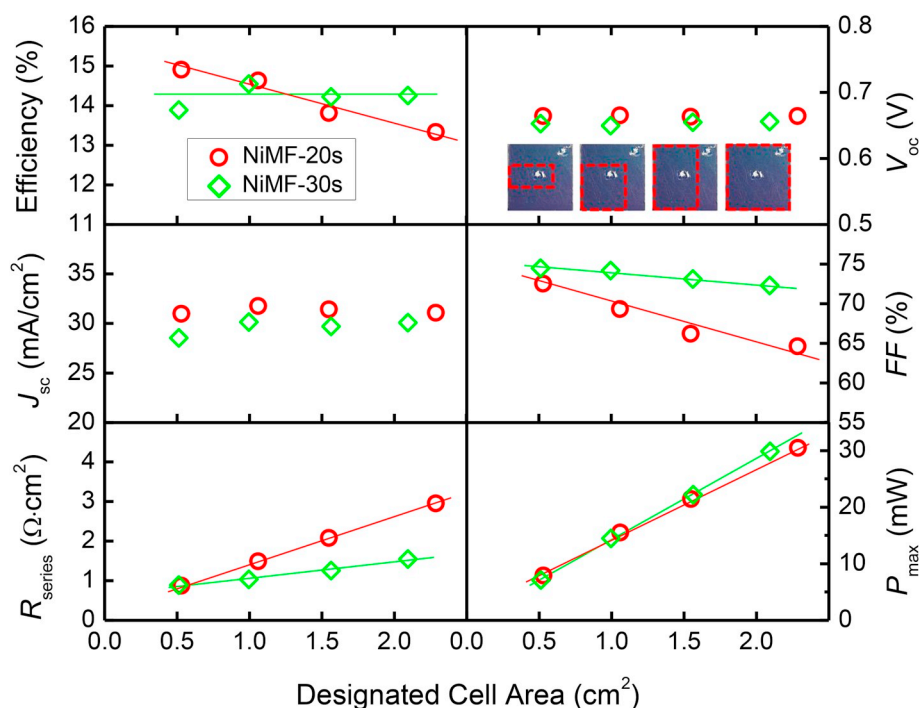


Fig. 5. Photovoltaic performance parameters of solar cells including NiMF-20s (red circle) and NiMF-30s (green diamond) depending on the designated cell area. The solar cell regions defined by mechanical scribing in each area are displayed in the inset with red dashed lines. (For interpretation of the references to colour in this figure legend, the reader is referred to the Web version of this article.)

conducting NiMFs significantly increased the number of pathways for carrier collection. Gridless CIGS thin-film solar cells exhibiting high photovoltaic performances were obtained by combining the NiMF with a light diffusive layer and a TCO thin film. The fiber thickness was controlled to obtain a better trade-off between the transmittance and R_{sh} . Thicker NiMF suppressed the degradation of the FF for larger solar cell areas because of the low resistance, while the thinner NiMF improved the transmittance, subsequently boosting the J_{sc} . The highly transparent and conductive NiMF can be a good substitute for patterned film grids to achieve the fabrication of efficient and aesthetically superior solar cells and modules. We expect that TCOs can be potentially replaced by NiMFs by further engineering.

Declarations of interest

None.

Acknowledgments

This work was supported by the Technology Development Program to Solve Climate Changes of the National Research Foundation (NRF) funded by the Ministry of Science, ICT & Future Planning (2016M1A2A2936754) and was also supported by the 'New & Renewable Energy' of a Korea Institute of Energy Technology Evaluation and Planning (KETEP) grant funded by the Ministry of Trade, Industry and Energy (20193010014830).

Appendix A. Supplementary data

Supplementary data to this article can be found online at <https://doi.org/10.1016/j.solmat.2019.109998>.

References

- [1] D.S. Hecht, L. Hu, G. Irvin, Emerging transparent electrodes based on thin films of carbon nanotubes, graphene, and metallic nanostructures, *Adv. Mater.* 23 (2011) 1482–1513.
- [2] S. Lee, J.S. Lee, J. Jang, K.-H. Hong, D.-K. Lee, S. Song, K. Kim, Y.-J. Eo, J.H. Yun, J. Gwak, C.-H. Chung, Robust nanoscale contact of silver nanowire electrodes to semiconductors to achieve high performance chalcogenide thin film solar cells, *Nano Energy* 53 (2018) 675–682.
- [3] S. De, T.M. Higgins, P.E. Lyons, E.M. Doherty, P.N. Nirmalraj, W.J. Blau, J.J. Boland, J.N. Coleman, Silver nanowire networks as flexible, transparent, conducting films: extremely high DC to optical conductivity ratios, *ACS Nano* 3 (2009) 1767–1774.
- [4] T.M. Barnes, M.O. Reese, J.D. Bergeson, B.A. Larsen, J.L. Blackburn, M.C. Beard, J. Bult, J. van de Lagemaat, Comparing the fundamental physics and device performance of transparent, conductive nanostructured networks with conventional transparent conducting oxides, *Adv. Energy Mater.* 2 (2012) 353–360.
- [5] Z. Wu, Z. Chen, X. Du, J.M. Logan, J. Sippel, M. Nikolou, K. Kamaras, J.R. Reynolds, D.B. Tanner, A.F. Hebard, A.G. Rinzler, Transparent, conductive carbon nanotube films, *Science* 305 (2004) 1273–1276.
- [6] S. Bae, H. Kim, Y. Lee, X. Xu, J.-S. Park, Y. Zheng, J. Balakrishnan, T. Lei, H. Ri Kim, Y.I. Song, Y.-J. Kim, K.S. Kim, B. Özyilmaz, J.-H. Ahn, B.H. Hong, S. Iijima, Roll-to-roll production of 30-inch graphene films for transparent electrodes, *Nat. Nanotechnol.* 5 (2010) 574–578.
- [7] D.S. Ghosh, T.L. Chen, V. Pruneri, High figure-of-merit ultrathin metal transparent electrodes incorporating a conductive grid, *Appl. Phys. Lett.* 96 (2010) 041109.
- [8] S.H. Kang, I.G. Kim, B.-N. Kim, J.H. Sul, Y.S. Kim, I.-K. You, Facile fabrication of flexible in-plane graphene micro-supercapacitor via flash reduction, *ETRI J.* 40 (2018) 275–282.
- [9] V. Garg, B.S. Sengar, V. Awasthi, A. Kumar, R. Singh, S. Kumar, C. Mukherjee, V.V. Atuchin, S. Mukherjee, Investigation of dual-ion beam sputter-instigated plasmon generation in TCOs: a case study of GZO, *ACS Appl. Mater. Interfaces* 10 (2018) 5464–5474.
- [10] A. Teymouri, S. Pillai, Z. Ouyang, X. Hao, F. Liu, C. Yan, M.A. Green, Low-temperature solution processed random silver nanowire as a promising replacement for indium tin oxide, *ACS Appl. Mater. Interfaces* 9 (2017) 34093–34100.
- [11] V. Awasthi, V. Garg, B.S. Sengar, S.K. Pandey, Aaryashree, S. Kumar, C. Mukherjee, S. Mukherjee, Impact of sputter-instigated plasmonic features in TCO films: for ultrathin photovoltaic applications, *Appl. Phys. Lett.* 110 (2017) 103903.
- [12] V. Scardaci, R. Coull, P.E. Lyons, D. Rickard, J.N. Coleman, Spray deposition of highly transparent, low-resistance networks of silver nanowires over large areas, *Small* 7 (2011) 2621–2628.
- [13] L. Hu, H.S. Kim, J.-Y. Lee, P. Peumans, Y. Cui, Scalable coating and properties of transparent, flexible, silver nanowire electrodes, *ACS Nano* 4 (2010) 2955–2963.
- [14] H. Peng, C. Xie, D.T. Schoen, Y. Cui, Large anisotropy of electrical properties in layer-structured In_2Se_3 nanowires, *Nano Lett.* 8 (2008) 1511–1516.
- [15] T. Kato, J.-L. Wu, Y. Hirai, H. Sugimoto, V. Bermudez, Record efficiency for thin-film polycrystalline solar cells up to 22.9% achieved by Cs-treated $\text{Cu}(\text{In,Ga})(\text{Se,S})_2$, *IEEE J. Photovolt.* 9 (2019) 325–330.
- [16] P. Jackson, R. Wuerz, D. Hariskos, E. Lotter, W. Witte, M. Powalla, Effects of heavy alkali elements in $\text{Cu}(\text{In,Ga})\text{Se}_2$ solar cells with efficiencies up to 22.6%, *Phys. Status Solidi RRL* 10 (2016) 583–586.
- [17] M. Powalla, M. Cernjak, J. Eberhardt, F. Kessler, R. Kniese, H.D. Mohring, B. Dimmler, Large-area CIGS modules: pilot line production and new developments, *Sol. Energy Mater. Sol. Cells* 90 (2006) 3158–3164.
- [18] F. Kessler, D. Herrmann, M. Powalla, Approaches to flexible CIGS thin-film solar cells, *Thin Solid Films* 480–481 (2005) 491–498.
- [19] K. Moriwaki, M. Nomoto, S. Yuuya, N. Murakami, T. Ohgoh, K. Yamane, S. Ishizuka, S. Niki, Monolithically integrated flexible $\text{Cu}(\text{In,Ga})\text{Se}_2$ solar cells and submodules using newly developed structure metal foil substrate with a dielectric layer, *Sol. Energy Mater. Sol. Cells* 112 (2013) 106–111.
- [20] Datasheet from ascent SOLAR web page, http://www.ascentsolar.com/downloads/ASTI_BareModules_LargeScaleGroup_datasheet.pdf, Accessed date: May 2019.
- [21] Product brochure from miasole web page, http://miasole.com/miasole2017/wp-content/uploads/2015/05/MiaSole_brochure_final.pdf, Accessed date: May 2019.
- [22] Product brochure from global solar web page, <http://www.globalsolar.com/sites/default/files/uploads/images/Copy%20of%20PowerFLEX%20BAPV%20Datasheet%20%28PROD%20LIT%20-%201000781%20-%201%20-%20D%29.PDF>, Accessed date: May 2019.
- [23] F. Fertig, R. Lantzsich, A. Mohr, M. Schaper, M. Bartzsch, D. Wissen, F. Kersten, A. Mette, S. Peters, A. Eidner, J. Cieslak, K. Duncker, M. Junghänel, E. Jarzembowski, M. Kauer, B. Faulwetter-Quandt, D. Meißner, B. Reiche, S. Geißler, S. Hörnlein, C. Klenke, L. Niebergall, A. Schönmann, A. Wehrauch, F. Stenzel, A. Hofmann, T. Rudolph, A. Schwabedissen, M. Gundermann, M. Fischer, J.W. Müller, D.J.W. Jeong, Mass production of p-type Cz silicon solar cells approaching average stable conversion efficiencies of 22 %, *Energy Procedia* 124 (2017) 338–345.
- [24] I. Repins, S. Glynn, J. Duenow, T.J. Coutts, W.K. Metzger, M.A. Contreras, Required material properties for high-efficiency CIGS modules, *Proc. SPIE* 7409, Thin Film Solar Technology, San Diego, CA, 2009, p. 74090M.
- [25] K.-S. Lee, M.G. Kang, Optimum design of dye-sensitized solar module for building-integrated photovoltaic systems, *ETRI J.* 39 (2017) 859–865.
- [26] J.L. Elechiguerra, L. Larios-Lopez, C. Liu, D. Garcia-Gutierrez, A. Camacho-Bragado, M.J. Yacamán, Corrosion at the Nanoscale: the case of silver nanowires and nanoparticles, *Chem. Mater.* 17 (2005) 6042–6052.
- [27] C.H. Liu, X. Yu, Silver nanowire-based transparent, flexible, and conductive thin film, *Nanoscale Res Lett* 6 (2011) 75.
- [28] H.-G. Im, J. Jin, J.-H. Ko, J. Lee, J.-Y. Lee, B.-S. Bae, Flexible transparent conducting composite films using a monolithically embedded AgNW electrode with robust performance stability, *Nanoscale* 6 (2014) 711–715.
- [29] X.Y. Zeng, Q.K. Zhang, R.M. Yu, C.Z. Lu, A new transparent conductor: silver nanowire film buried at the surface of a transparent polymer, *Adv. Mater.* 22 (2010) 4484–4488.
- [30] H.S. Jo, S. An, J.-G. Lee, H.G. Park, S.S. Al-Deyab, A.L. Yarin, S.S. Yoon, Highly flexible, stretchable, patternable, transparent copper fiber heater on a complex 3D surface, *SPG Asia Mater.* 9 (2017) e347.
- [31] S. An, Y.I. Kim, H.S. Jo, M.-W. Kim, M.W. Lee, A.L. Yarin, S.S. Yoon, Silver-decorated and palladium-coated copper-electroplated fibers derived from electrospun polymer nanofibers, *Chem. Eng. J.* 327 (2017) 336–342.
- [32] S. An, H.S. Jo, D.Y. Kim, H.J. Lee, B.K. Ju, S.S. Al-Deyab, J.H. Ahn, Y. Qin, M.T. Swihart, A.L. Yarin, S.S. Yoon, Self-junctioned copper nanofiber transparent flexible conducting film via electrospinning and electroplating, *Adv. Mater.* 28 (2016) 7149–7154.
- [33] W.-J. Lee, D.-H. Cho, J.-H. Wi, W.S. Han, B.-K. Kim, S.D. Choi, J.-Y. Baek, Y.-D. Chung, Characterization of bilayer AZO film grown by low-damage sputtering for $\text{Cu}(\text{In,Ga})\text{Se}_2$ solar cell with a CBD-ZnS buffer layer, *Mater. Sci. Semicond. Process.* 81 (2018) 48–53.
- [34] J.-H. Wi, D.-H. Cho, W.-J. Lee, W.S. Han, Y.-D. Chung, Effects of Ga concentration in $\text{Cu}(\text{In,Ga})\text{Se}_2$ thin film solar cells with a sputtered-Zn(O,S) buffer layer, *Sol. Energy* 145 (2017) 59–65.
- [35] J.H. Wi, T.G. Kim, J.W. Kim, W.J. Lee, D.H. Cho, W.S. Han, Y.D. Chung, Photovoltaic performance and interface behaviors of $\text{Cu}(\text{In,Ga})\text{Se}_2$ solar cells with a sputtered-Zn(O,S) buffer layer by high-temperature annealing, *ACS Appl. Mater. Interfaces* 7 (2015) 17425–17432.
- [36] D.-H. Cho, W.-J. Lee, S.-W. Park, J.-H. Wi, W.S. Han, J. Kim, M.-H. Cho, D. Kim, Y.-D. Chung, Non-toxically enhanced sulfur reaction for formation of chalcogenide thin films using a thermal cracker, *J. Mater. Chem.* 2 (2014) 14593–14599.
- [37] D.-H. Cho, K.-S. Lee, Y.-D. Chung, J.-H. Kim, S.-J. Park, J. Kim, Electronic effect of Na on $\text{Cu}(\text{In,Ga})\text{Se}_2$ solar cells, *Appl. Phys. Lett.* 101 (2012) 023901.
- [38] W.J. Lee, H.J. Yu, J.H. Wi, D.H. Cho, W.S. Han, J. Yoo, Y. Yi, J.H. Song, Y.D. Chung, Behavior of photocarriers in the light-induced metastable state in the p-n heterojunction of a $\text{Cu}(\text{In,Ga})\text{Se}_2$ solar cell with CBD-ZnS buffer layer, *ACS Appl. Mater. Interfaces* 8 (2016) 22151–22158.
- [39] D. Stauffer, Scaling theory of percolation clusters, *Phys. Rep.-Rev. Sec. Phys. Lett.* 54 (1979) 1–74.
- [40] J. van de Groep, P. Spinelli, A. Polman, Transparent conducting silver nanowire networks, *Nano Lett.* 12 (2012) 3138–3144.
- [41] E.J. Menke, M.A. Thompson, C. Xiang, L.C. Yang, R.M. Penner, Lithographically patterned nanowire electrodeposition, *Nat. Mater.* 5 (2006) 914–919.
- [42] A.F. Mayadas, M. Shatzkes, Electrical-resistivity model for polycrystalline films: the case of arbitrary reflection at external surfaces, *Phys. Rev. B* 1 (1970) 1382–1389.
- [43] G. Haacke, New figure of merit for transparent conductors, *J. Appl. Phys.* 47 (1976) 4086–4089.
- [44] P.J. King, U. Khan, M. Lotya, S. De, J.N. Coleman, Improvement of transparent conducting nanotube films by addition of small quantities of graphene, *ACS Nano* 4 (2010) 4238–4246.
- [45] J. Zou, H.-L. Yip, S.K. Hau, A.K.Y. Jen, Metal grid/conducting polymer hybrid transparent electrode for inverted polymer solar cells, *Appl. Phys. Lett.* 96 (2010) 203301.
- [46] P.N. Nirmalraj, P.E. Lyons, S. De, J.N. Coleman, J.J. Boland, Electrical connectivity in single-walled carbon nanotube networks, *Nano Lett.* 9 (2009) 3890–3895.
- [47] C. Hunger, K.D.M. Rao, R. Gupta, C.R. Singh, G.U. Kulkarni, M. Thelakkat, Transparent metal network with low haze and high figure of merit applied to front and back electrodes in semitransparent ITO-free polymer solar cells, *Energy Technol.* 3 (2015) 638–645.
- [48] J.-H. Wi, W.S. Han, W.-J. Lee, D.-H. Cho, H.-J. Yu, C.-W. Kim, C. Jeong, J.H. Yun, C.-I. Kim, Y.-D. Chung, Spectral response of $\text{CuGaSe}_2/\text{Cu}(\text{In,Ga})\text{Se}_2$ monolithic tandem solar cell with open-circuit voltage over 1 V, *IEEE J. Photovolt.* 8 (2018) 840–848.
- [49] V.K. Jain, A.P. Kulshreshtha, Indium-Tin-Oxide transparent conducting coatings on silicon solar cells and their “figure of merit”, *Sol. Energy Mater.* 4 (1981) 151–158.
- [50] M.A. Green, K. Emery, Y. Hishikawa, W. Warta, E.D. Dunlop, Solar cell efficiency tables (version 39), *Prog. Photovoltaics Res. Appl.* 20 (2012) 12–20.
- [51] C. van Lare, G. Yin, A. Polman, M. Schmid, Light coupling and trapping in ultrathin $\text{Cu}(\text{In,Ga})\text{Se}_2$ solar cells using dielectric scattering patterns, *ACS Nano* 9 (2015) 9603–9613.
- [52] J. Krc, M. Sever, A. Campa, Z. Lokar, B. Lipovsek, M. Topic, Optical confinement in chalcopyrite based solar cells, *Thin Solid Films* 633 (2017) 193–201.
- [53] K.S. Lee, Y.D. Chung, N.M. Park, D.H. Cho, K.H. Kim, J. Kim, S.J. Kim, Y. Kim, S.K. Noh, Analysis of the current-voltage curves of a $\text{Cu}(\text{In,Ga})\text{Se}_2$ thin-film solar cell measured at different irradiation conditions, *J. Opt. Soc. Korea* 14 (2010) 321–325.
- [54] M.A. Green, Chapter 8. Design of silicon solar cells, in: J. Nick Holonyak (Ed.), *Solar Cells: Operating Principles, Technology, and System Applications*, Prentice-Hall, Inc., Englewood Cliffs, N.J., USA, 1982, pp. 145–147.